

RESEARCH ARTICLE

10.1002/2017JA024366

Key Points:

- Martian ionosphere exhibits considerable variability during quiet Sun period
- Dominant source of ionospheric variability is found to be variations in CO₂ densities
- CO₂ variability is caused by wave-2 nonmigrating tides associated with surface

Supporting Information:

- Supporting Information S1

Correspondence to:

C. Narvaez,
cnarvaez@bu.edu

Citation:

Mendillo, M., Narvaez, C., Vogt, M. F., Mayyasi, M., Forbes, J., Galand, M., ... Andersson, L. (2017). Sources of ionospheric variability at Mars. *Journal of Geophysical Research: Space Physics*, 122. <https://doi.org/10.1002/2017JA024366>

Received 16 MAY 2017

Accepted 7 JUL 2017

Accepted article online 30 AUG 2017

Sources of Ionospheric Variability at Mars

Michael Mendillo¹ , Clara Narvaez¹ , Marissa F. Vogt¹ , Majd Mayyasi¹ , Jeffrey Forbes² , Marina Galand³ , Edward Thiemann⁴ , Mehdi Benna⁵, Francis Eparvier⁴, Phillip Chamberlin⁵, Paul Mahaffy⁵, and Laila Andersson⁴ 

¹Center for Space Physics, Boston University, Boston, MA, USA, ²Department of Aerospace Engineering, University of Colorado Boulder, Boulder, CO, USA, ³Department of Physics and Astronomy, Imperial College London, London, UK, ⁴Laboratory for Space and Atmospheric Physics, University of Colorado Boulder, Boulder, CO, USA, ⁵Goddard Space Flight Center, NASA, Greenbelt, MD, USA

Abstract During the Mars Atmosphere and Volatile Evolution (MAVEN) mission's deep-dip #2 campaign of 17–22 April 2015, spacecraft instruments observed all of the physical parameters needed to assess the photo-chemical-equilibrium (PCE) explanation for ionospheric variability at a fixed altitude (135 km) near the peak of the Martian ionosphere. MAVEN measurements of electron density, electron temperature, neutral CO₂ density, and solar irradiance were collected during 28 orbits. When inserted into the PCE equation, the measurements of varying PCE drivers correlated with the observed electron density variations to within instrumental uncertainty levels. The dominant source of this positive correlation was the variability of CO₂ densities associated with the longitudinal wave-2 component of nonmigrating tides in the Martian thermosphere.

1. Introduction

Prior to the arrival of the Mars Atmosphere and Volatile Evolution (MAVEN) mission to Mars, the basic structure and variability of the Martian ionosphere had been studied by three types of observations: (a) radio occultation experiments from several missions, (b) in situ probes by the two Viking landers, and (3) the radar experiments on Mars Express (MEX) and Mars Reconnaissance Orbiter (MRO). The Mars Advanced Radar for Subsurface and Ionosphere Sounding (MARSIS) instrument on MEX continues to provide large data sets for (a) electron density profiles above the height of maximum density and (b) integrals of electron density profiles, i.e., total electron content (TEC) data. The MEX radio occultation experiments also continue to produce electron density profiles $N_e(h)$. Finally, the SHARAD (SHALLOW RADAR) experiment on the Mars Reconnaissance Orbiter is a second major source of TEC data (Campbell & Watters, 2016). Comprehensive reviews of pre-MAVEN ionospheric observations and models appear in Withers (2009), Haider et al. (2011), and Haider and Mahajan (2014).

With the exception of the two Viking landers, none of the ionospheric measurements mentioned above was accompanied by simultaneous in situ observations of neutral and plasma compositions and temperatures. This lack of information about atmospheric parameters needed to understand ionospheric processes resulted in virtually all prior studies of ionospheric variability at Mars to consider the only forcing parameter that could be measured—solar flux changes observed from Earth. These include solar proxies such as the $F_{10.7}$ radio flux or direct spectral irradiance measurements from the Extreme Ultraviolet Variability Experiment on the Solar Dynamics Observatory or the Thermosphere, Ionosphere Energetics and Dynamics (TIMED)-Solar Extreme Ultraviolet Experiment (SEE). A very substantial yield came from these studies of solar-induced variability associated with the full range of time scales of solar activity. These included (a) solar flare effects (Gurnett et al., 2005, 2008; Lollo et al., 2012; Mendillo et al., 2006) on time scales of minutes, (b) day-to-day solar irradiance effects (Martinis et al., 2003; Mendillo et al., 2003, 2011; Rishbeth & Mendillo, 2004), (c) monthly solar active regions (Mendillo et al., 2013a; Venkateswara Rao et al., 2014; Withers & Mendillo, 2005), and (d) solar cycle time frames (Mendillo et al., 2013a, 2016; Sanchez-Cano et al., 2015; Withers et al., 2015). The MAVEN mission, with its suite of plasma, neutral atmosphere, and solar measurements, overcame the limitation of studying ionospheric variability at Mars by using only solar observations from Earth.

Here we describe the first MAVEN-based study of ionospheric variability using a comprehensive set of solar, atmospheric, and plasma parameters. To do so, we select an altitude where plasma dynamics is not important

($h = 135$ km), and thus, a closed set of internal parameters can be used within the theoretical framework of photo-chemical-equilibrium (PCE). MAVEN's 6 day observational campaign of 17–22 April 2015 was the second of its “deep-dip” observing periods when periapse was lowered from its nominal height of ~ 150 km to a height in the 125–130 km range. The deep-dip #2 orbits provided the optimal conditions for a rigorous application of PCE principles—midday hours near the subsolar point—under quiet Sun conditions. The initial report of in situ observations during this period showed substantial variability in the neutral atmosphere (Figure 5 in Bougher et al., 2015). Our first study of ionospheric observations during this period used total ion density observations that had not yet been fully calibrated, and their magnitudes were consistently below predictions from the Mars Initial Reference Ionosphere model (Mendillo et al., 2015). Nevertheless, their orbit-by-orbit relative variabilities were reliable, as shown in Table S1 (supporting information) in Mendillo et al. (2015), and they pointed to the need of follow-up studies. We now relate fully calibrated solar observations, neutral atmosphere densities, and ionospheric electron densities and electron temperatures made by MAVEN during its deep-dip #2 campaign of April 2015. With 28 orbital passes encountering the 135 km altitude point on either side of periapse, the MAVEN observations offer the functional equivalent of 56 Viking lander data sets—but with much improved instrumentation and the first ever solar observations made from Mars.

2. Observations

MAVEN's observations during the 17–22 April 2015 period occurred when Mars was at orbital longitudes (L_s) of $\sim 330^\circ$, corresponding to northern hemisphere spring, and a distance from the Sun of ~ 1.48 AU. MAVEN's orbit has inclination = 75° and period = 4.5 h. This results in 5.47 orbits per day with similar, but not identical, samplings in latitude and local time (and therefore solar zenith angle). This campaign provides all of the crucial data sets required to assess photo-chemical-equilibrium (PCE) values of electron density. To do so, we select a height of 135 km to ensure that PCE theory is fully applicable. As shown in many modeling studies, plasma dynamics starts to become important at heights above ~ 170 km (e.g., see Figure 16 in Mendillo et al., 2011, and references therein). A study at ~ 135 km is essentially equivalent to a study at the height of daytime maximum electron density (h_{\max} is typically ~ 125 – 130 km), and thus, our findings have direct relevance to the dominant component (M_2 layer) of the Martian ionosphere.

The data sets we use at 135 km come from MAVEN's following instruments: (a) the Neutral Gas and Ion Mass Spectrometer (NGIMS) measurements of the abundance of the major constituent of the Martian neutral atmosphere that is ionized (CO_2) (Mahaffy et al., 2014), (b) the Langmuir Probe and Wave (LPW) values of electron density and electron temperature (Andersson et al., 2015), and (c) the Solar Extreme Ultraviolet Monitor (EUVM) first ever observations of the solar irradiance (flux versus wavelength) at Mars. Given that EUVM does not make its full set of observations at periapse heights near 130 km, we will assess solar input via a combination of key wavelengths observed, model representations, and calculations of photon absorption with altitude (Eparvier et al., 2015; Thiemann et al., 2017). The satellite ephemeris provides the solar zenith angle (SZA) at 135 km for each of the orbits, with all altitudes quoted using areodetic heights.

During a deep-dip campaign, MAVEN instruments operate to an altitude approximately two atmospheric scale heights lower than during a nominal periapse orbit, and thus, denser neutral atmospheres and ionospheres are sampled. In situ instrument performance can be affected under such conditions, and thus, we will treat the inbound encounters of 135 km separately from the outbound encounters of the same altitude. Our goal of studying individual parameter variability at similar latitudes and local times is thus preserved by this approach. For example, while the calibration of NGIMS CO_2 values to absolute values (“accuracy”) can have an uncertainty of $\leq 20\%$ for inbound/outbound orbit segments, their relative orbit-to-orbit uncertainty values (“precision”) are smaller ($< 5\%$). Moreover, as will be described below, we will average the three consecutive values spanning 135 km and that reduces the uncertainty further.

3. Context and Goals

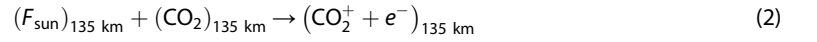
The relevance of the MAVEN observations to ionospheric PCE conditions arises from the processes at 135 km for plasma production (P), loss (L), and motion (M). As described in many textbooks (Pröls, 2004; Ratcliffe,

1960; Rishbeth & Garriot, 1969; Schunk & Nagy, 2009), PCE systems are well understood, and so only the briefest of reviews will be sufficient for our purposes:

$$\text{ionospheric continuity equation: } \frac{dN_e}{dt} = P + L + M \quad (1)$$

where P , L , and M denote changes due to solar production, chemical loss, and plasma motion.

For ionospheric production (P), the solar flux reaching 135 km ($F_{\text{sun}})_{135 \text{ km}}$ ionizes the CO_2 there



followed by rapid ion transformation chemistry:



yielding a plasma of O_2^+ and e^- at 135 km.

$$\text{ionospheric chemical loss (L): } \text{O}_2^+ + e^- \xrightarrow{\alpha} \text{O} + \text{O} \quad (4)$$

occurs at 135 km with a reaction rate (loss coefficient) α .

As we shall see, while MAVEN instruments can provide the neutral and plasma parameters at 135 km, solar irradiances are available only for "top of the atmosphere" conditions ($F_{\text{sun}})_{\text{top}}$. As a first approximation, we will assume that $(F_{\text{sun}})_{135 \text{ km}}$ is a constant fraction of $(F_{\text{sun}})_{\text{top}}$ for the 6 days of quiescent solar conditions. Combining that constant with all of the photochemical constants related to cross sections, ionization efficiencies, and scale height into a single constant (K) and denoting solar flux as simply F_{sun} , we get the following representational conditions of PCE at 135 km:

$$P = \frac{dN_e}{dt} = K \times F_{\text{sun}} \times \cos(\text{SZA}) \times n(\text{CO}_2) \quad (5)$$

$$L = -\frac{dN_e}{dt} = -\alpha N_e N(\text{O}_2^+) \cong -\alpha N_e^2, \quad (6)$$

where F_{sun} is the subsolar point flux and $\cos(\text{SZA})$ accounts for nonsubsolar conditions near the production peak (Fox & Yeager, 2006; Rishbeth & Garriot, 1969). Charge neutrality results in $N(\text{O}_2^+) \sim N_e$ and the loss coefficient is

$$\alpha = 2.4 \times 10^{-7} (300/T_e)^{0.7} \quad (7)$$

(Schunk & Nagy, 2009).

For ionospheric conditions where plasma dynamics is negligible (as found in the dense neutral atmosphere near 135 km), and for time periods when the electron density is not changing rapidly (as found for midday conditions), both the dN_e/dt and M terms in equation (1) are approximately zero. This defines the formal photo-chemical-equilibrium (PCE) condition to be $|P| = |L|$, and thus, equating (5) and (6) gives

$$\begin{aligned} N_e^2 &= K \times \frac{F_{\text{sun}} \cos(\text{SZA}) n(\text{CO}_2) (T_e)^{0.7}}{2.4 \times 10^{-7} (300)^{0.7}} \\ &= \text{Constant} \times F_{\text{PCE}} \end{aligned} \quad (8)$$

where

$$\text{constant} = \frac{K}{2.4 \times 10^{-7} (300)^{0.7}} \quad (9)$$

and

$$F_{\text{PCE}} = F_{\text{sun}} \cos(\text{SZA}) n(\text{CO}_2) (T_e)^{0.7} \quad (10)$$

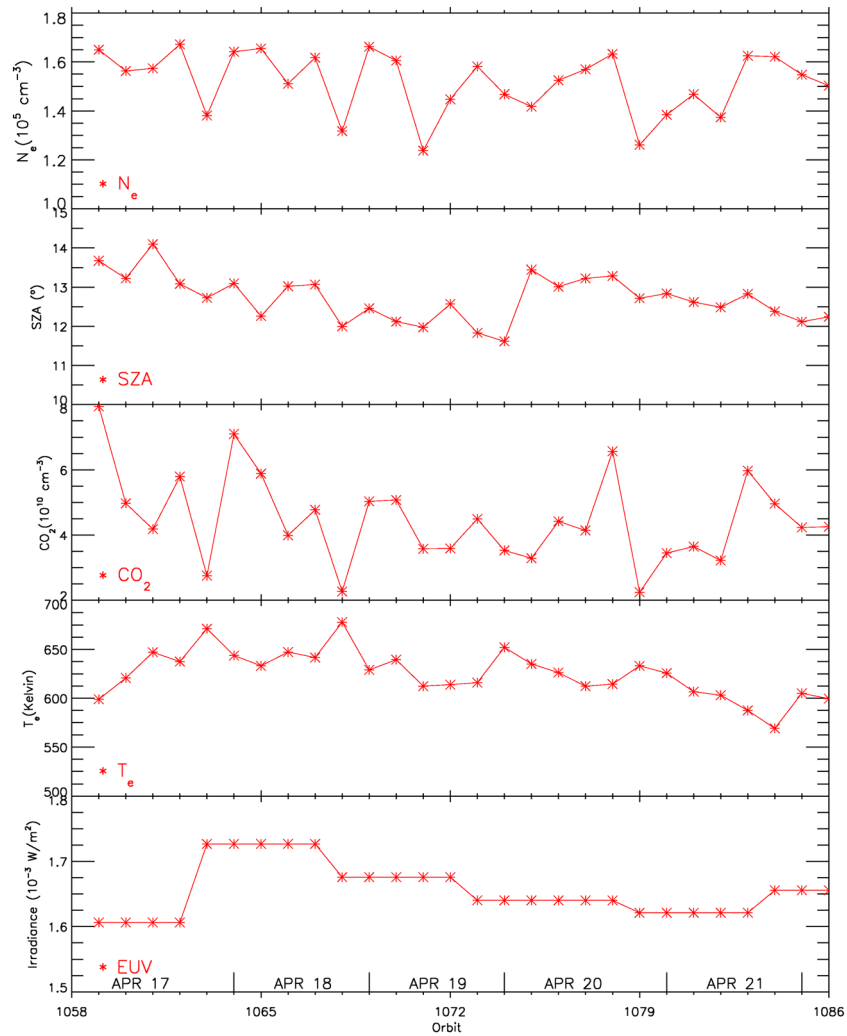


Figure 1. (first to fifth panels) Values of N_e , SZA, CO_2 , T_e , and irradiance for outbound orbits 1058 through 1086 during the deep dip campaign of April 2015. Typically, five to six orbits occur each day, as shown on the lower axis.

with F_{sun} at the top of the atmosphere and SZA, $n(\text{CO}_2)$, and T_e measured at 135 km where the electron density N_e is observed.

This results in the specific PCE condition to test using five parameters provided by MAVEN data sets:

$$N_e^2 \sim F_{\text{PCE}} \tag{11}$$

4. Analysis

4.1. Testing Photo-Chemical-Equilibrium Conditions

For each of the 28 MAVEN deep-dip #2 orbits, there are two sets of observations at a fixed height of 135 km—those before and after periapse. The parameters used from LPW and NGIMS are N_e , T_e , and $n(\text{CO}_2)$ at a specific SZA. For the solar irradiance, we used the MAVEN Level-3 data product of daily values derived from EUV irradiance observations summed over the wavelength range of 5 to 90 nm (CO_2 is ionized at wavelengths less than 90.04 nm). Since we are dealing with the M_2 layer of the Martian ionosphere, the soft X-ray wavelength below 5 nm was not used (they penetrate to ~ 110 km to form the M_1 layer, as recently discussed in Mendillo et al. (2017)). As described above, we decided to treat the inbound/outbound observations as independent

Table 1
Averages of Measured Parameters (Figure 1) With Their Standard Deviations in Units and Percent Deviations

Parameter	Average	Standard deviation	Percent deviation
Electron Density ($e^- \text{ cm}^{-3}$)	1.5×10^5	1.3×10^4	8.2%
Solar Zenith Angle (deg)	12.7	0.6	4.6%
CO ₂ Density ($\text{CO}_2 \text{ cm}^{-3}$)	4.5×10^{10}	1.4×10^{10}	30.7%
Electron Temperature (K)	625.0	24.0	3.8%
Irradiance (W/m^2)	1.7×10^{-3}	4.1×10^{-5}	2.5%
[Electron Density ($e^- \text{ cm}^{-3}$)] ²	2.3×10^{10}	3.7×10^9	15.9%
cos (SZA)	0.975	0.002	0.2%
(T_e) ^{0.7}	90.6	2.4	2.6%

data sets as a check on results obtained. A benefit of the outbound observations was that they were all clustered about the equator with $\langle \text{latitude} \rangle = -0.2^\circ \pm 0.5^\circ$, while the inbound data have $\langle \text{latitude} \rangle = -7.4^\circ \pm 2.4^\circ$. As will be shown in later sections (Figures 5–7), regions sampled have a good distribution in longitude but do not include the latitudes (30°–90°S) of strongest crustal magnetic fields within the 150°–210°E longitude region and ionospheric variability associated with them (Mendillo et al., 2013b).

We thus begin with outbound data at 135 km averaged from the three values spanning 135 km (typically covering ~2 km). Figure 1 portrays the 28 orbit-by-orbit outbound values for N_e , SZA, $n(\text{CO}_2)$, T_e , and solar EUV. Table 1 summarizes their mean values and standard deviations (top rows), while the bottom three rows give values for the functional dependences actually used for N_e and SZA in equation (10), i.e., N_e^2 , $\cos(\text{SZA})$, and $T_e^{0.7}$.

Inserting the parameters shown in Figure 1, orbit by orbit, into equation (10) tests the anticipated linear relationship between N_e^2 and the PCE factor of equation (11). The results are shown in Figure 2, with different symbols used to indicate the dates of observations. There is a strong correlation clearly present between the PCE driving parameters and their resulting electron densities, with a linear correlation coefficient = 0.85 (with outliers included here and in Tables 1 and 2 discussed in the caption).

In the supporting information, we provide results for the inbound data sets at 135 km (Figures S1 and S2).

To explore the contributions of each parameter to the overall correlation, we used the 28 values of a given parameter (as shown in Figure 1) in conjunction with constant values for its three companion parameters (i.e., the sample averages from Table 1). The parameter-correlation results are summarized in Table 2. As is evident visually from Figure 1, the neutral density of the primary ionized species (CO_2) is the strongest

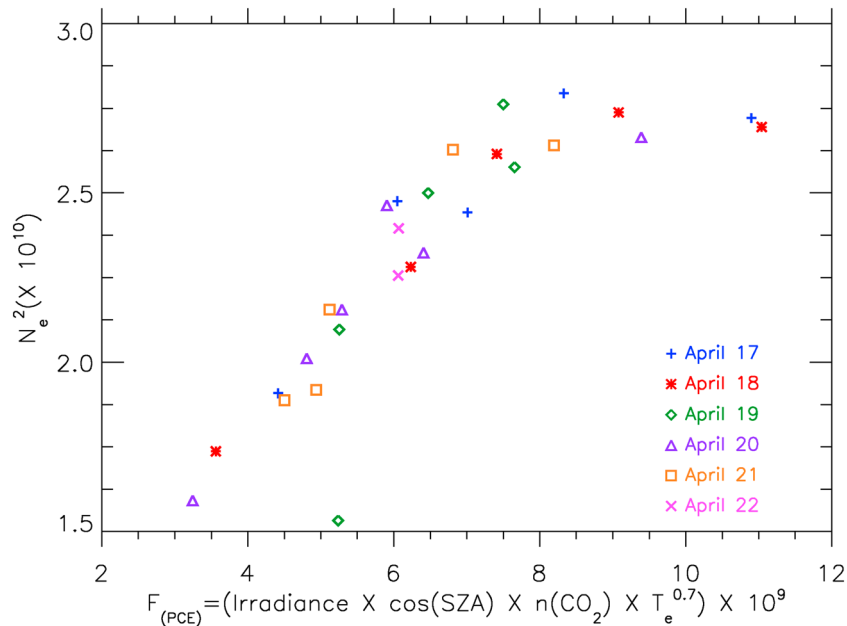


Figure 2. Comparison of squared values of the electron density (N_e) observed by the LPW instrument with the product of the four variables defined by the PCE factor (F_{PCE}) (see text and equations (10) and (11)). The observations for F_{PCE} come from LPW (T_e), NGIMS (CO_2), and EUVM (irradiance), with SZA provided by the MAVEN ephemeris. Different symbols are used to indicate the dates of observations. The outlier (low) value on 19 April 2015 occurred when a solar wind enhancement caused a dramatic lowering of the ionopause ($h \sim 240$ km), as noted in a prior study (Mendillo et al., 2017), probably introducing dynamical effects upon local PCE conditions. The two (N_e)² values associated with the highest PCE factors correspond to the first values on April 17 and 18 in Figure 1. At present we are unable to determine if the two N_e observations are anomalously low, if the two CO_2 observations are anomalously high, or reasons exist for non-PCE behavior.

Table 2
PCE Parameter Sensitivity Summary

Parameters that vary daily	Correlation coefficient
All	0.85
cos(SZA)	-0.29
$n(\text{CO}_2)$	0.84
T_e	-0.24
Irradiance	0.04

contributor, dominating the overall correlation. (During MAVEN's subsequent deep-dip #4 campaign of September 2015, Vogt et al. (2017) also found CO_2 to dominate variability under extreme solar terminator conditions (SZA = 89°–94°) at midlatitudes (~45°S).) The solar irradiance changes shown in Table 2 contributed the least to variability, as anticipated from Figure 1. The small changes in small SZAs result in a negative correlation of no actual statistical significance (1σ for $\langle \cos(\text{SZA}) \rangle = 0.2\%$ in Table 1). The dependence of N_e on T_e via the chemical recombination loss process (equation (7)) provides an unanticipated result of a negative correlation to be discussed in more detail below.

To show the consistency between the inbound and outbound sets of observations, their independent correlation results between N_e^2 and the PCE factors can be summarized as follows:

(inbound data—with a correlation coefficient of 0.88):

$$N_e^2 \left[10^{10} (\text{e}^-/\text{cm}^3)^2 \right] = 1.01 + 2.06 \left(\text{irradiance} \times \cos(\text{SZA}) \times n(\text{CO}_2) \times (T_e)^{0.7} \right) \quad (12)$$

(outbound data—with a correlation coefficient of 0.85):

$$N_e^2 \left[10^{10} (\text{e}^-/\text{cm}^3)^2 \right] = 1.29 + 1.58 \left(\text{irradiance} \times \cos(\text{SZA}) \times n(\text{CO}_2) \times (T_e)^{0.7} \right) \quad (13)$$

(All data—with a correlation coefficient of 0.85):

$$N_e^2 \left[10^{10} (\text{e}^-/\text{cm}^3)^2 \right] = 1.19 + 1.74 \left(\text{irradiance} \times \cos(\text{SZA}) \times n(\text{CO}_2) \times (T_e)^{0.7} \right) \quad (14)$$

The overall conclusion is that PCE conditions are well applied at 135 km, with the dominance of CO_2 variability being the key parameter that accounts for N_e variability during this period of solar quiescent conditions.

4.2. A Closer Look at Solar Irradiances

MAVEN is the first satellite at Mars to make detailed observations of the Sun's ultraviolet emissions directly related to the physics of the Martian upper atmosphere and ionosphere. In our analysis above, we used one of the EUVM's data products to characterize the photon flux versus wavelength at the top of the Martian atmosphere for each of the 6 days of the deep-dip #2 campaign. We assumed that the irradiance reaching 135 km was a relatively constant fraction of the topside fluxes. The irradiances were summed over the wavelength range 5–90 nm as subsolar values (Figure 1, fifth panel), with solar zenith angle effects shown separately (second panel), in order to assess their different contributions via equations (10) and (11). Here we explore a refinement to that approach by computing the fluxes that reach 135 km for each orbit. We use the NGIMS profiles of major atmospheric constituents (CO_2 , N_2 , O, and CO) for each outbound orbit segment, together with their absorption and ionization cross sections, to calculate photon degradation versus wavelength from 350 km down to a height of 135 km, (Thiemann et al., 2017). While the EUVM instrument did not take measurements during some of the early orbits (#1058–1065), 21 of the 28 orbits could be used. For some of the orbits (1066–1069 and 1083–1086) only a daily average was possible. The results are shown in Figure 3. The computational scheme takes into account changing solar zenith angles with height, and thus, the data points in Figure 3 give summed irradiance (0.1–93 nm) at the top of the atmosphere (black asterisks) and at 135 km within the atmosphere (green squares).

There are several items to note.

1. The values for top of the atmosphere are similar to the combined effects in Figure 1 (second and fifth panels).
2. The values at 135 km have lower magnitudes by a ratio of 0.87. This corresponds to an optical depth of $\tau \sim 0.2$, consistent with a subsolar production maximum below 135 km (Martinis et al., 2003; Mayyasi & Mendillo, 2015).

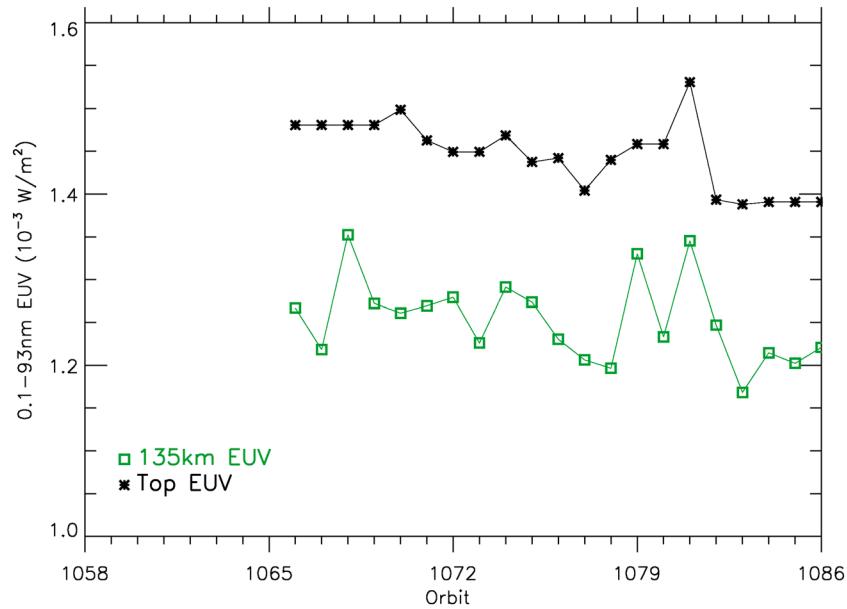


Figure 3. Comparison of irradiance values at the top of the ionosphere (black asterisks) and at 135 km (green squares) for orbits 1066 to 1086. For each orbit, the degradation of photon fluxes versus wavelength through the observed atmosphere is calculated following methods described in Thiemann et al. (2017) (see text).

- Using the 21 irradiance values (denoted EUV) at 135 km in place of the $F_{\text{sun}} \times \cos(\text{SZA})$ terms in equation (10), the correlation equation (11) becomes

$$N_e^2 [10^{10} (e^- / \text{cm}^3)^2] = 0.84 + 3.06 (\text{EUV} \times n(\text{CO}_2) \times (T_e)^{0.7}) \quad (15)$$

with the associated Figure S3 in the supporting information. The correlation coefficient increased from 0.845 (i.e., when using daily values in equation (13) and their minor variations shown in Table 1) to 0.870 here with orbit-by-orbit values.

We conclude that conducting our correlation analysis using orbit-by-orbit calculations of the solar irradiance reaching the satellite height of 135 km does indeed result in an improvement over using daily values of irradiance at the top of the atmosphere. Yet the number of orbits that could be handled in this way suffered a reduction of 25% (28 to 21). Given the modest difference in the correlations and 6 days of relatively quiet Sun conditions, it is preferable to use the larger data set of 28 orbit parameters in the analyses to follow.

4.3. Variability Beyond PCE Conditions

The strong correlation shown in Figure 2 still exhibits variability beyond that portrayed by the linear relationship in equation (13). We computed the departures from the linear fit in Figure 2 and show these in Figure 4. Note that we keep to the use of electron density squared as defined by equation (11). The results thus describe the overall variability (6.3%) of N_e^2 due to the influence of non-PCE drivers, as well as to uncertainties in the measurements. Removal of the outlier value reduces the average observed departure from PCE conditions from 6.3% to 5.5%. Thus, an average departure of ~6% for N_e^2 leads to an average departure of N_e from PCE condition to be ~3%. Uncertainties of 3% are within observational capabilities, and thus, we consider all forms of variability accounted for in this PCE data set. Of course, this conclusion pertains to this particular period of observations that occurred during a 6 day span of very minor solar variability.

5. Discussion

5.1. Application of PCE Theory

As described by equation (8), the derivation of the PCE equation relating observed electron density to its solar and atmospheric drivers is most appropriate for midday conditions (when $dN_e/dt \sim 0$). It should be least appropriate for solar terminator regions when dN_e/dt achieves maximum positive (at dawn) and maximum

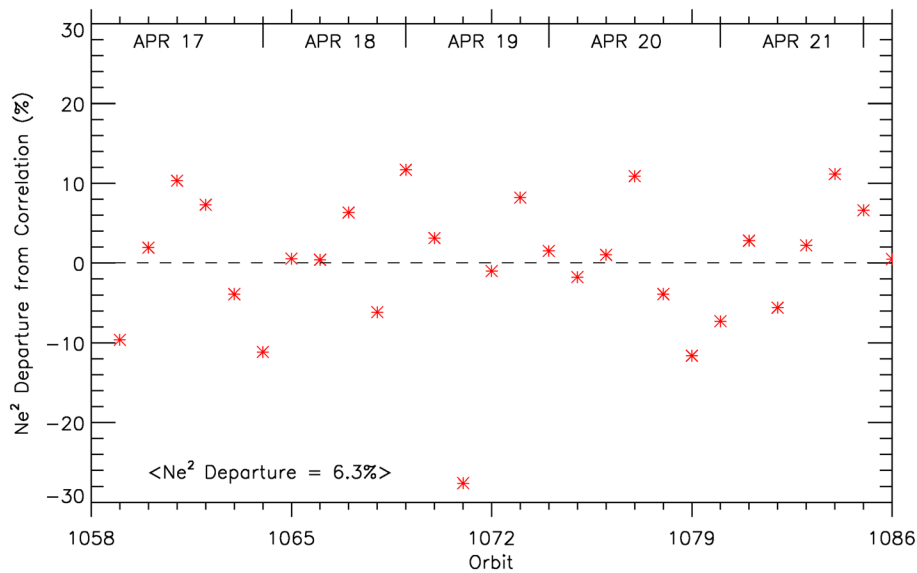


Figure 4. The departures of (electron density)² from its linear relationship to PCE conditions depicted in Figure 2. The average value is 6.3%. If the outlier value discussed in Figure 2 for orbit #1071 (19 April 2015) is omitted, the average departure becomes 5.5%. The same analysis using the inbound data appears in Figure S4 in the supporting information.

negative (at dusk) values. Yet prior to the radio remote sensing observations from the radar experiments (MARSIS) on MEX and MAVEN's new in situ data, the vast majority of ionospheric studies relied upon radio occultation experiments (ROX) that occurred close to the terminators. One of the many results that came from ROX data sets was that the maximum electron density of the Martian ionosphere did not correlate particularly well with solar drivers when the solar radio flux proxy ($F_{10.7}$) was used. As shown in equation (8), N_e should correlate with $[\text{flux (subsolar)} \cos(\text{SZA})]^\gamma$, where $\gamma = 0.50$. It became common to compare the various reports of $\gamma \neq 0.5$ from different sets of observations (e.g., Hantsch & Bauer, 1990), perhaps giving the impression (erroneously) that the PCE law's dominance at h_{max} needed re-evaluation. Similar results occurred for Titan's ionosphere, for example, with $\gamma = 0.54$ reported by Edberg et al. (2013). Girazian and Withers (2013) summarized the results from many past studies for Mars and found that published values of γ have ranged from 0.24 to 0.44, with an average of 0.35 when $F_{10.7}$ was used. Such issues existed in spite of earlier warnings of the poor correlations between actual EUV data and $F_{10.7}$ (Hinteregger, 1981). When Girazian and Withers (2013) re-analyzed ROX data using actual solar irradiance values from the TIMED-SEE instrument (using 2903 Mars Global Surveyor (MGS) profiles with $\text{SZA} = 71\text{--}80^\circ$), the PCE value of $\gamma = 0.5$ was obtained. This points out that PCE conditions can be used even during periods of rapid change (sunrise/sunset) because the time constant for chemical loss ($\tau_c = (\alpha N_e)^{-1}$ approximately a few minutes) is still much smaller than that for plasma diffusion at heights below ~ 170 km (Fox & Yeager, 2006; Mendillo et al., 2011).

For conditions where plasma dynamics is imposed upon the ionosphere, for example, from enhanced solar wind flow, plasma can be moved horizontally across the sunrise/sunset meridians (Cui et al., 2015a; Withers et al., 2012). Under such conditions, the topside shapes of $N_e(h)$ profiles might depart from PCE predictions (Mendillo et al., 2017). Similarly, when Cui et al. (2015b) took into account changes in electron temperature across the terminator, they derived a value of $\gamma = 0.55$. In this study, we avoided all such questionable applications of PCE theory by examining observations at a height (135 km) where both vertical and horizontal transport would be minimal and at midday periods ($\text{SZA} = 4^\circ\text{--}10^\circ$) when $dN_e/dt \sim 0$. The conformity of observations with PCE theory was found to be robust to within the accuracy limits of MAVEN's instruments.

5.2. Role of Electron Temperature

Perhaps, the most unanticipated aspect of our study was the minimal influence of electron temperature upon the PCE solution for electron density. Two major findings about electron temperatures have become

apparent from multiple MAVEN studies: (1) T_e values near the peak of the ionosphere are often in the 600–700 K range, more than a factor of 2 above previous estimates using Viking data merged with the assumption of thermal equilibrium ($T_e = T_i = T_n$) at the height of peak electron density (see review in Matta et al., 2014) and (2) an anticorrelation is often found between electron densities and electron temperatures (Ergun et al., 2015; Vogt et al., 2017). In its simplest form, PCE theory predicts a positive correlation between N_e and T_e that arises from the T_e dependence in the recombination rate of O_2^+ and e^- , as shown in the derivation leading to equation (8). A warm electron population recombines with O_2^+ more slowly than would occur with a cooler electron gas, and thus, N_e remains high (Cui et al., 2015b; Withers et al., 2014; Vogt et al., 2017). While that is certainly true, quantitatively it is a small effect. For example, with $N_e \sim (T_e)^{0.35}$ from equation (8), values of N_e change by $<\pm 3\%$ when T_e changes from 650 K by ± 50 K, well within the observational accuracies possible for T_e and N_e .

A full treatment of the multiple competing processes that determine the electron temperature at Mars appears in Matta et al. (2014, and earlier studies referenced therein). For a fixed source of electron heating, the resultant T_e depends upon the number of electrons available to share that heat. Thus, low N_e densities have the highest T_e values (and vice versa). Hence, a steady state solution leads to an anticorrelation between N_e and T_e . Competing with this plasma heat-sharing process is an important loss of electron heat via collisions with neutral gases. As shown in Matta et al. (2014) and as recently discussed in MAVEN-based studies, the major heat loss mechanism for electrons arises from their collisions with the highly abundant CO_2 molecules. Thus, our findings of N_e correlated with CO_2 via the photoionization process, while N_e is simultaneously anticorrelated with T_e due to enhanced collisional cooling when CO_2 is more abundant, are both in agreement with basic PCE and thermal balance processes.

5.3. Dynamical Role of CO_2

A previous modeling study by Martinis et al. (2003) dealt with Martian ionospheric variability arising from day-to-day changes in solar activity. The MGS data set they selected had Mars in opposition so that solar fluxes measured at Earth could be applied at Mars with only the (distance)⁻² correction. Holding the neutral atmosphere constant for 17 days, the daily changes in the Sun's XUV irradiance were used to calculate day-to-day electron density profiles, $N_e(h)$. The N_{max} values from those model profiles gave a variability of $\pm 6\%$, while the MGS radio occultation profiles showed an observed variability $\pm 5\%$. This agreement suggested that if day-to-day changes in solar irradiance could account for all of the observed variability, any changes in other parameters (e.g., CO_2 concentrations and electron temperatures) at the height of unit optical depth must have been minimal.

In the present study, we explored the opposite situation: when MAVEN had observational evidence that solar variability was very small for the 6 day period 17–22 April 2015, there were nevertheless considerable variations in electron density at a fixed height (135 km), constant latitude (equatorial), and identical local time (noon). Virtually all of this variability was driven by changes in the dominant neutral gas (CO_2) that was ionized at 135 km. In this section we describe the origin of these CO_2 changes that account for electron density variations produced under photo-chemical-equilibrium conditions.

Starting with Figure 1, the third panel gave the time history (orbit by orbit) of CO_2 densities observed during MAVEN's outbound encounters of $h = 135$ km. There is an apparent randomness to the pattern, with only the slightest hint that a maximum or minimum value occurs (roughly) every third point or so. With MAVEN having an orbit of ~ 4.5 h, three consecutive samplings occur close to the semidiurnal cadence. An alternate way of portraying the same data is to plot them versus longitude, and that is done in Figure 5. In Figure 5 (top), the data points are identified by daily codes and (even with only 28 observations) a double-cycle ("wave-2") pattern can be inferred. Figure 5 (middle) shows average $\langle CO_2 \rangle$ values versus longitude, while Figure 5 (bottom) shows that pattern in percent change from the mean. In each of these representations a wave-2 pattern is clearly present.

The existence of a wave-2 longitudinal variation in a measurement of Mars' atmosphere from a quasi Sun-synchronous platform like MAVEN is not unexpected. It is linked to the dominance of wave-2 topography at low latitudes (Forbes & Hagan, 2000; Moulden & Forbes, 2008; Withers et al., 2003), which, in turn, modulates the thermal excitation of tides near Mars' surface. The dominant tide producing this effect is the eastward propagating diurnal tide with zonal wave number $s = -1$ (DE1), which is in near-resonance in Mars' atmosphere (Zurek, 1988). See the appendix for tide terminology. In addition to the large wave-2 variation

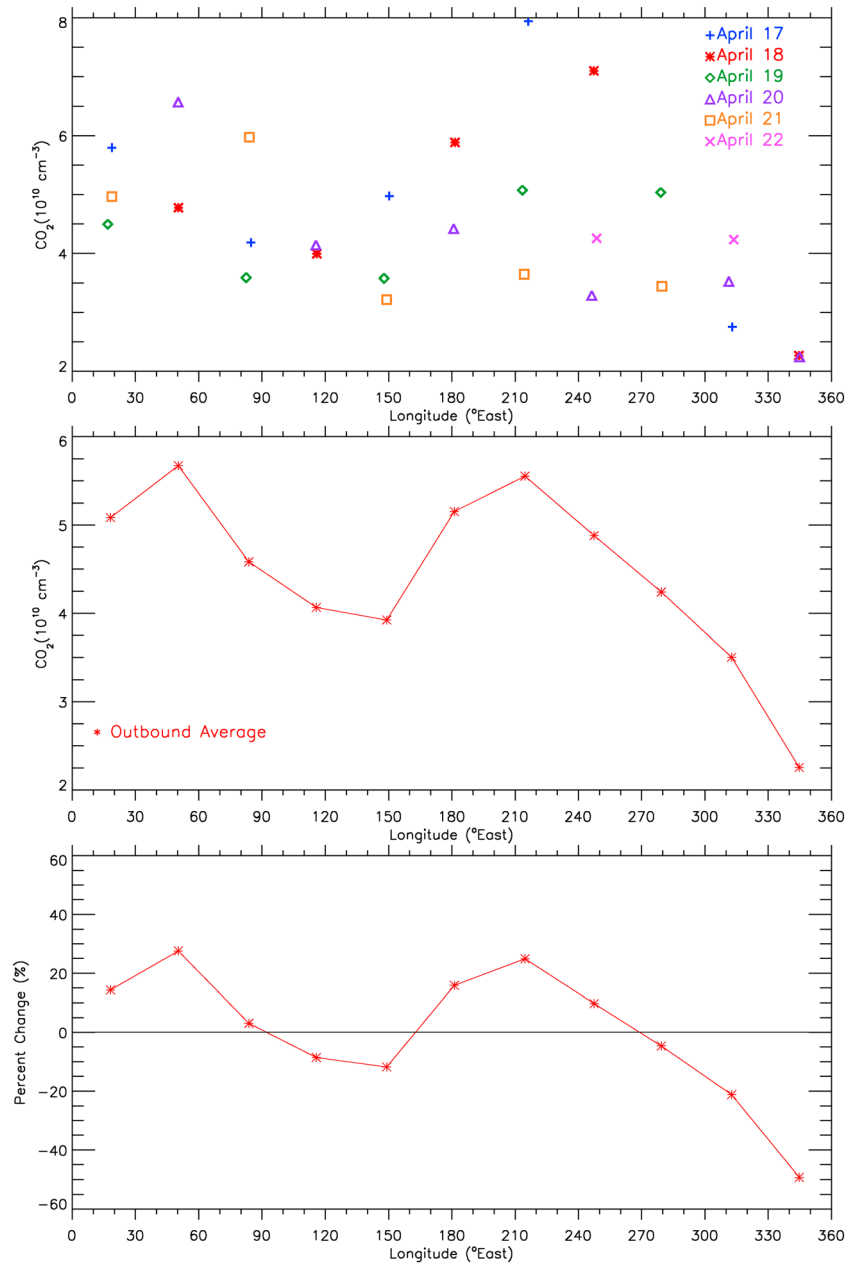


Figure 5. The distribution of CO₂ densities versus longitude for outbound orbits. (top) Data points with symbols to indicate date of observation. (middle) Averages of the points in top panel versus longitude. (bottom) Percent deviations of the points in the middle panel with respect to their sample average. Figure 7 (next section) will show a similar analysis for the inbound data set described in the supporting information.

in thermosphere density seen in near-equatorial Mars Global Surveyor (MGS) data (e.g., Withers et al., 2003), analyses of MAVEN data also reveal a strong wave-2 structure (England et al., 2016; Lo et al., 2015). For instance, limb-scan observations with the Imaging Ultraviolet Spectrograph analyzed by Lo et al. (2015) showed that along the equator the derived CO₂ densities revealed a strong wave-2 component (their Figures 2 and 3). The peak densities occurred at 75°E and 225°E, with amplitudes approaching the 30% levels shown in our Figure 5. Furthermore, an examination of solar fluxes verifies that variable thermosphere heating is not a source of the observed CO₂ density variations in Figure 1. We thus conclude that the ionospheric variability shown in Figure 1 (first panel) is due to PCE processes at 135 km driven by CO₂ variability associated with nonmigrating tides.

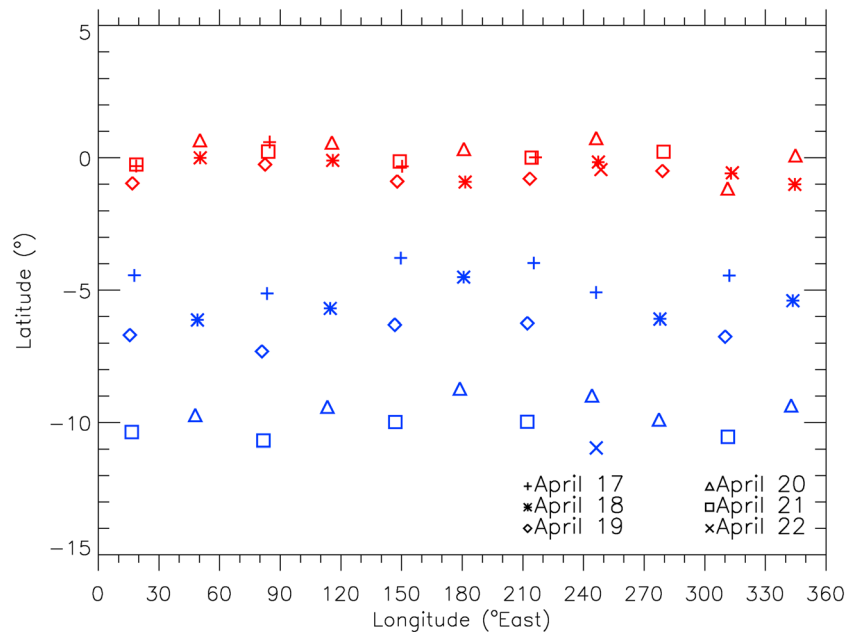


Figure 6. Locations of MAVEN's measurements of CO_2 densities at 135 km during the period 17–22 April 2015. All observations pertain to local noon (near subsolar) conditions. Different symbols are used for each day, with red for outbound and blue for inbound data. Note that the outbound points are all clustered near the equator, while the inbound points are near 5°S for 17–19 April and near $\sim 10^\circ\text{S}$ for 20–22 April (see text).

5.4. Ionospheric Production Within a Thermosphere With Nonmigrating Tides

As described in section 3, the electron densities observed by LPW are in charge neutrality with O_2^+ even though the initial ions formed are CO_2^+ . Thus, production of CO_2^+ is essentially equal to the electron production rate. Seth et al. (2006) conducted modeling studies of the tidal influence upon CO_2^+ production and found that the dominant effect was a wave-4 pattern, followed in magnitude by wave-2 effects. Their simulations were done to match MGS observations conducted at higher latitudes ($50^\circ\text{--}70^\circ\text{N}$) and for larger solar zenith angles ($\sim 78^\circ$) than in our study ($\sim 0^\circ$ latitude and $\text{SZA} \sim 13^\circ$). Nevertheless, this prompted us to examine the inbound data shown in the supporting information collected at latitudes somewhat south of the equator ($\sim 5^\circ\text{--}10^\circ\text{S}$ and $\text{SZA} \sim 7^\circ$) to search for tidal influences away from the equator.

Figure 6 shows the latitude-longitude distribution of all available NGIMS observations of CO_2 at 135 km during the 6 day campaign. The symbols are the same as used in previous figures to denote dates, with outbound points in red and inbound in blue. As discussed above, the 28 outbound data points are all clustered near the equator ($0.2^\circ\text{S} \pm 0.5^\circ$). The 28 inbound points fall between 4° and 11°S (average $\sim 7^\circ\text{S} \pm 2.4^\circ$), with two subgroups: 17–19 and April 20–22 April. These have average latitudes of $\sim 5^\circ\text{S}$ and $\sim 10^\circ\text{S}$, respectively. Figure 7 gives the CO_2 density values (top), their variability patterns in percent at $\sim 5^\circ\text{S}$, $\sim 10^\circ\text{S}$ (middle), and their overall average variability in percent (bottom). These are to be compared with results from the outbound passes shown in Figure 5. The CO_2 density values show a mild latitude gradient away from the equator (top). More surprising are the percent variability patterns in Figure 7 (middle and bottom). There is clearly a departure from the well-defined wave-2 pattern seen at the equator. This transition from a wave-2 to a wave-4 pattern occurs over a surprisingly small range of latitudes. The average amplitude in percent for the inbound data set (Figure 7, bottom) is about half that found for the outbound data at the equator (Figure 5, bottom).

Consistent with the above MAVEN results, Withers et al. (2003) found a significant ($\sim 18\%$) wave-4 component in MGS accelerometer data at 130 km near $L_s = 60^\circ$ and between -15° and $+15^\circ$ latitude (their Figure 8). Similar to the situation at Earth (Forbes et al., 2008; Truskowski et al., 2014), Mars general circulation models (Angelats i Coll et al., 2004; Moudzen & Forbes, 2008) indicate that wave-4 in Mars' thermosphere is attributable to DE3 and SE2 tidal components associated with wave-4 topography. Since these waves can coexist at low latitudes, it is plausible that interference effects between them can produce abrupt changes in total

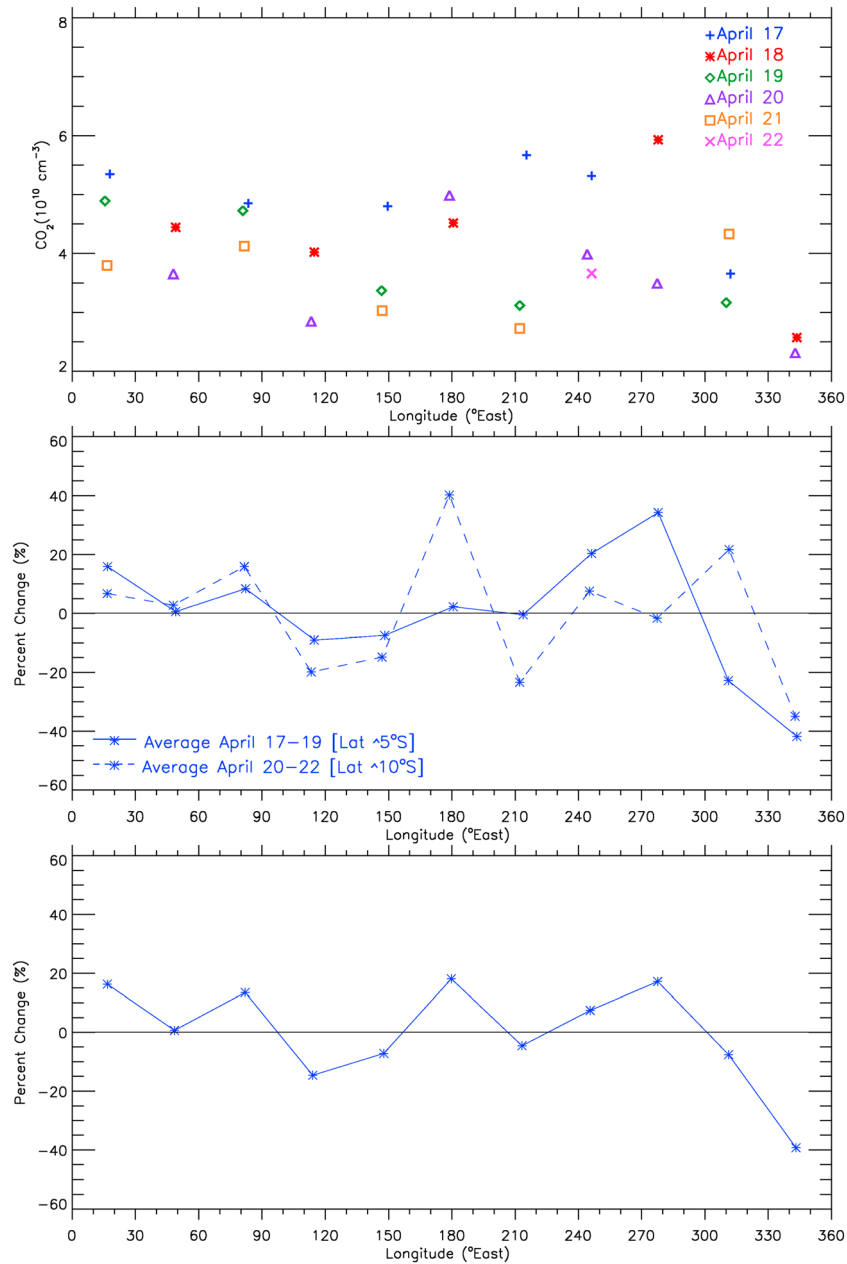


Figure 7. Longitude distribution of MAVEN's CO₂ observations at 135 km made during the inbound orbit segments of 17–22 April 2015. (top) The CO₂ densities using the same daily symbols as in Figure 5. (middle) The average variability patterns using percent changes from mean values for the subsets of data near 5°S and 10°S, respectively. (bottom) The overall average variability (in percent) using all data points. The persistently low values at longitude ~345°E in Figures 5 and 7 will be the topic of a separate study.

wave-4 amplitude with latitude similar to that seen in our MAVEN observations, depending on local time, longitude and season.

Finally, while considerable research has been conducted on tidal effects within the Martian ionosphere, the observational parameter most often examined was the height of maximum electron density, $h_m M_2$ (e.g., Bougher et al., 2001; Cahoy et al., 2006). The tidal signatures upon $h_m M_2$ are altitude peaks and troughs versus longitude resulting from expansion and contractions of the neutral atmosphere. From PCE theory, the height of unit optical depth (approximately peak ionospheric production) thus varies—but not the maximum electron density ($N_m M_2$). Here we examined the electron density at a *fixed* height (135 km) and the tidal signatures appeared clearly in the observed electron densities.

6. Summary and Conclusions

We have analyzed a set of MAVEN observations that provided an optimal test of photo-chemical-equilibrium processes in the Martian ionosphere. Our findings for the period of 17–22 April 2015 are as follows:

1. During a 6 day time span of very low solar variability, the electron density (N_e) at a fixed height (135 km) near the peak of the Martian ionosphere showed orbit-to-orbit variability ($\sigma \approx 8\%$) during midday conditions close to the subsolar latitude.
2. The major driver for the observed N_e variability was found to be the changing densities of CO_2 that are ionized to form the ionosphere.
3. Variations in electron temperature (T_e) were observed to be anticorrelated with the electron densities; variations in the T_e -dependent loss rate were shown to be negligible.
4. The T_e variability was anticorrelated with CO_2 densities and thus explained by variable cooling of the electron gas to changing CO_2 densities.
5. With changes in solar flux, solar zenith angle, and electron temperature all secondary sources of variability for this period, the observed changes in CO_2 densities versus longitude illuminated the strong role that nonmigrating tides in the thermosphere can have upon ionospheric variability.
6. Additional studies using the more abundant data for heights above 135 km can probe the altitude extent of PCE conditions for different seasons, latitudes, and local times.
7. MAVEN's multiparameter observations during low activity portions of the solar cycle set important baseline conditions that will help understand the more dramatic changes in the ionosphere that occur during flare and coronal mass ejection events.

Appendix A: Tide Terminology

A spectrum of thermal tides is forced in a rotating planetary atmosphere by the absorption of solar radiation. Each spectral component is periodic in time and longitude with a frequency $n\Omega$ that is a subharmonic of the planetary rotation rate ($\Omega = 2\pi \text{ sol}^{-1}$) where $n = 1, 2, 3$, etc. refers to diurnal, semidiurnal, terdiurnal, etc., and an integer zonal wave number (s) that is positive (negative) for tides propagating to the west (east). The notation DWs(SWs) or DEs(SEs) is often used to denote a westward or eastward propagating diurnal(semidiurnal) tide, respectively, with zonal wave number = s . From a Sun-synchronous (constant local time) perspective, the longitudinal structure that is seen has a longitudinal wave number equal to $|s - n|$ (Forbes & Hagan, 2000) and is due to the presence of *nonmigrating* tides ($s \neq n$), i.e., those that do not migrate with the apparent motion of the Sun to a ground-based observer (Chapman & Lindzen, 1970).

Acknowledgments

At Boston University, this work was supported, in part, by grant and contract funding from the MAVEN mission for M. Mendillo, C. Narvaez, M.F. Vogt, and M. Mayyasi and by sabbatical support for M. Mendillo from Boston University. J. M. F. acknowledges support through NASA award NNX16AJ39G from the Mars Data Analysis Program. Work at Imperial College London is supported by STFC of UK under grants ST/K001051/1 and ST/N000692/1. We acknowledge the data analysis work conducted by BU undergraduate research assistant Michaela Moynihan during summer 2016. All of the MAVEN data used in this study can be publicly found through the Planetary Plasma Interactions node of NASA's Planetary Data System at <http://ppi.pds.nasa.gov/>.

References

- Andersson, L., Ergun, R. E., Delory, G. T., Eriksson, A., Westfall, J., Reed, H., ... Meyers, D. (2015). The Langmuir Probe and Waves (LPW) instrument for MAVEN. *Space Science Reviews*, 195, 173–198. <https://doi.org/10.1007/s11214-015-0194-3>
- Angelats i Coll, M., Forget, F., López-Valverde, M. A., Read, P. L., & Lewis, S. R. (2004). Upper atmosphere of Mars up to 120 km: Mars Global Surveyor accelerometer data analysis with the LMD general circulation model. *Journal of Geophysical Research*, 109, E01011. <https://doi.org/10.1029/2003JE002163>
- Bougher, S., Engel, S., Hinson, D., & Forbes, J. (2001). Mars Global Surveyor Radio Science electron density profiles: Neutral atmosphere implications. *Geophysical Research Letters*, 28(16), 3091–3094. <https://doi.org/10.1029/2001GL012884>
- Bougher, S., Jakosky, B., Halekas, J., Grebowsky, J., Luhmann, J., Mahaffy, P., ... Yelle, R. (2015). Early MAVEN deep dip campaign reveals thermosphere and ionosphere variability. *Science*, 350, 6261. <https://doi.org/10.1126/science.aad0459>
- Cahoy, K., Hinson, D., & Tyler, G. (2006). Radio science measurements of atmospheric refractivity with Mars Global Surveyor. *Journal of Geophysical Research*, 111, E05003. <https://doi.org/10.1029/2005JE002634>
- Campbell, B., & Watters, T. (2016). Phase compensation of MARSIS subsurface sounding and estimation of ionospheric properties: New insights from SHARAD results. *Journal of Geophysical Research: Planets*, 121, 180–193. <https://doi.org/10.1002/2015JE004917>
- Chapman, S., & Lindzen, R. (1970). *Atmospheric Tides*. Dordrecht, Netherlands: D. Reidel Press.
- Cui, J., Galand, M., Yelle, R., Wei, Y., & Zhang, S.-J. (2015a). Day-to-night transport in the Martian ionosphere: Implications from total electron content measurements. *Journal of Geophysical Research: Space Physics*, 120, 2333–2346. <https://doi.org/10.1002/2014JA020788>
- Cui, J., Galand, M., Zhang, S., Vigren, E., & Zou, H. (2015b). The electron thermal structure in the dayside Martian ionosphere implied by the MGS radio occultation data. *Journal of Geophysical Research: Planets*, 120, 278–286. <https://doi.org/10.1002/2014JE004726>
- Edberg, N. J. T., Andrews, D. J., Shebanits, O., Ågren, K., Wahlund, J.-E., Opgenoorth, H. J., ... Girazian, Z. (2013). Solar cycle modulation of Titan's ionosphere. *Journal of Geophysical Research: Space Physics*, 118, 5255–5264. <https://doi.org/10.1002/jgra.50463>
- England, S. L., Lui, G., Withers, P., Yigit, E., Lo, D., Jain, S., ... Jakosky, B. M. (2016). Simultaneous observations of atmospheric tide from combined in situ and remote observations at Mars from the MAVEN spacecraft. *Journal of Geophysical Research: Planets*, 121, 594–607. <https://doi.org/10.1002/2016JE004997>
- Eparvier, F. G., Chamberlin, P. C., Woods, T. N., & Thiemann, E. M. B. (2015). The Solar Extreme Ultraviolet Monitor for MAVEN. *Space Science Reviews*, 195, 293–301. <https://doi.org/10.1007/s11214-015-0195-2>

- Ergun, R. E., Morooka, M. W., Andersson, L. A., Fowler, C. M., Delory, G. T., Andrews, D. J., ... Jakosky, B. M. (2015). Dayside electron temperature and density profiles at Mars: First results from the MAVEN Langmuir probe and waves instrument. *Geophysical Research Letters*, *42*, 8846–8853. <https://doi.org/10.1002/2015GL065280>
- Forbes, J. M., & Hagan, M. E. (2000). Diurnal Kelvin wave in the atmosphere of Mars: Towards an understanding of “stationary” density structures observed by the MGS accelerometer. *Geophysical Research Letters*, *27*, 3563–3566. <https://doi.org/10.1029/2000GL011850>
- Forbes, J. M., Zhang, X., Palo, S., Russell, J., Mertens, C. J., & Mlynczak, M. (2008). Tidal variability in the ionospheric dynamo region. *Journal of Geophysical Research*, *113*, A02310. <https://doi.org/10.1029/2007JA012737>
- Fox, J. L., & Yeager, K. E. (2006). Morphology of the near-terminator Martian ionosphere: A comparison of models and data. *Journal of Geophysical Research*, *111*, A10309. <https://doi.org/10.1029/2006JA011697>
- Girazian, Z., & Withers, P. (2013). The dependence of peak electron density in the ionosphere of Mars on solar irradiance. *Geophysical Research Letters*, *40*, 1960–1964. <https://doi.org/10.1002/grl.50344>
- Gurnett, D., Kirchner, D. L., Huff, R. L., Morgan, D. D., Persoon, A. M., Averkamp, T. F., ... Picardi, G. (2005). Radar soundings of the ionosphere of Mars. *Science*, *310*, 1929–1933.
- Gurnett, D., Huff, R. L., Morgan, D. D., Persoon, A. M., Averkamp, T. F., ... Kirchner, D. L. (2008). An overview of radar soundings of the Martian ionosphere from the Mars Express spacecraft. *Advances in Space Research*, *41*, 1335–1346. <https://doi.org/10.1016/j.asr.2007.01.062>
- Haider, S., & Mahajan, K. (2014). Lower and upper ionosphere of Mars. *Space Science Reviews*, *182*, 19–84. <https://doi.org/10.1007/s11214-014-0058-2>
- Haider, S., Mahajan, K., & Kallio, E. (2011). Mars ionosphere: A review of experimental results and modeling studies. *Reviews of Geophysics*, *49*, RG4001. <https://doi.org/10.1029/2011RG000357>
- Hantsch, M., & Bauer, S. (1990). Solar control of the Mars ionosphere. *Planetary and Space Science*, *38*, 539–542.
- Hinteregger, H. E. (1981). Representations of solar EUV fluxes for aeronomical applications. *Advances in Space Research*, *1*(12), 39–52.
- Lo, D. Y., Yelle, R. V., Schneider, N. M., Jain, S. K., Stewart, A. I. F., England, S. L., ... Deighan, J. I. (2015). Non-migrating tides in the Martian atmosphere as observed by MAVEN IUVS. *Geophysical Research Letters*, *42*, 9057–9063. <https://doi.org/10.1002/2015GL066268>
- Lollo, A., Withers, P., Fallows, K., Girazian, Z., Matta, M., & Chamberlin, P. C. (2012). Numerical simulations of the ionosphere of Mars during a solar flare. *Journal of Geophysical Research*, *117*, A05314. <https://doi.org/10.1029/2011JA017399>
- Mahaffy, P. R., Benna, M., King, T., Harpold, D. N., Arvey, R., Barciniak, M., ... Bendt, M. (2014). The neutral gas and ion mass spectrometer on the Mars atmosphere and volatile evolution mission. *Space Science Reviews*, *195*, 49–73. <https://doi.org/10.1007/s11214-014-0091-1>
- Martinis, C. R., Wilson, J. K., & Mendillo, M. J. (2003). Modeling day-to-day ionospheric variability on Mars. *Journal of Geophysical Research*, *108*(A10), 1383. <https://doi.org/10.1029/2003JA009973>
- Matta, M., Galand, M., Moore, L., Mendillo, M., & Withers, P. (2014). Numerical simulations of ion and electron temperatures in the ionosphere of Mars: Multiple ions and diurnal variations. *Icarus*, *227*, 78–88. <https://doi.org/10.1016/j.icarus.2013.09.006>
- Mayyasi, M., & Mendillo, M. (2015). Why the Viking descent probes found only one ionospheric layer at Mars. *Geophysical Research Letters*, *42*, 7359–7365. <https://doi.org/10.1002/2015GL065575>
- Mendillo, M., Smith, S., Wroten, J., Rishbeth, H., & Hinson, D. (2003). Simultaneous Ionospheric Variability on Earth and Mars. *Journal of Geophysical Research*, *108*(A12), 1432. <https://doi.org/10.1029/2003JA009961>
- Mendillo, M., Withers, P., Hinson, D., Rishbeth, H., & Reinisch, B. (2006). Effects of solar flares on the ionosphere of Mars. *Science*, *311*, 1135–1138. <https://doi.org/10.1126/science.112209>
- Mendillo, M., Lollo, A., Withers, P., Matta, M., Pätzold, M., & Tellmann, S. (2011). Modeling Mars' ionosphere with constraints from same-day observations by Mars Global Surveyor and Mars Express. *Journal of Geophysical Research*, *116*, A11303. <https://doi.org/10.1029/2011JA016865>
- Mendillo, M., Marusiak, A., Withers, P., Morgan, D., & Gurnett, D. (2013a). A new semi-empirical model of the peak electron density of the Martian ionosphere. *Geophysical Research Letters*, *40*, 5361–5365. <https://doi.org/10.1002/2013GL057631>
- Mendillo, M., Narvaez, C., Withers, P., Matta, M., Kofman, W., & Mouginit, J. (2013b). Variability in ionospheric total electron content at Mars. *Planetary and Space Science*, *86*, 117–129. <https://doi.org/10.1016/j.pss.2013.08.010>
- Mendillo, M., Narvaez, C., Matta, M., Vogt, M., Mahaffy, P., Benna, M., & Jakosky, B. (2015). MAVEN and the Mars Initial Reference Ionosphere model. *Geophysical Research Letters*, *42*, 9080–9086. <https://doi.org/10.1002/2015GL065732>
- Mendillo, M., Trovato, J., Narvaez, C., Mayyasi, M., Moore, L., Vogt, M. F., ... Martinis, C. (2016). Comparative aeronomy: Molecular ionospheres at Earth and Mars. *Journal of Geophysical Research: Space Physics*, *121*(10), 10,269–10,288. <https://doi.org/10.1002/2016JA023097>
- Mendillo, M., Narvaez, C., Vogt, M. F., Mayyasi, M., Mahaffy, P., Benna, M., ... Jakosky, B. (2017). MAVEN and the total electron content of the Martian ionosphere. *Journal of Geophysical Research: Space Physics*, *122*, 3526–3537. <https://doi.org/10.1002/2016JA023474>
- Moudden, Y., & Forbes, J. M. (2008). Topographic connections with density waves in Mars' aerobraking regime. *Journal of Geophysical Research*, *113*, E11009. <https://doi.org/10.1029/2008JE003107>
- Prölss, G. (2004). *Physics of the Earth's Space Environment: An Introduction*. Berlin: Springer.
- Ratcliffe, J. (1960). *Physics of the Upper Atmosphere*. New York: Academic Press.
- Rishbeth, H., & Garriot, O. (1969). *Introduction to Ionospheric Physics*. NY: Academic Press.
- Rishbeth, H., & Mendillo, M. (2004). Ionospheric layers of Mars and Earth. *Planetary and Space Science*, *52*, 849–852. <https://doi.org/10.1016/j.pss.2004.02.007>
- Sanchez-Cano, B., Morgan, D. D., Witasse, O., Radicella, S. M., Herraiz, M., Orosei, R., ... Quinsac, G. (2015). Total electron content in the Martian atmosphere: A critical reassessment of the Mars Express MARSIS data sets. *Journal of Geophysical Research: Space Physics*, *120*, 2166–2182. <https://doi.org/10.1002/2014JA020630>
- Schunk, R. W., & Nagy, A. F. (2009). *Ionospheres* (2nd Ed.). New York: Cambridge University Press.
- Seth, S., Brahmananda Rao, V., Esprito Santo, C., Haider, S., & Choksi, V. (2006). Zonal variations of peak ionization rates in upper atmosphere of Mars at high latitude using Mars Global Surveyor accelerometer data. *Journal of Geophysical Research*, *111*, A09308. <https://doi.org/10.1029/2006JA011753>
- Thiemann, E., Chamberlin, P. C., Eparvier, F. G., Templeman, B., Woods, T. N., Bougher, S. W., & Jakosky, B. M. (2017). The MAVEN EUVM model of solar irradiance variability at Mars: Algorithms and results. *Journal of Geophysical Research: Space Physics*, *122*, 2748–2767. <https://doi.org/10.1002/2016JA023512>
- Truskowski, A. O., Forbes, J. M., Zhang, X., & Palo, S. E. (2014). New perspectives on thermosphere tides—1. Lower thermosphere spectra and seasonal-latitudinal structures. *Earth, Planets and Space*, *66*, 136. <https://doi.org/10.1186/s40623-014-0136-4>
- Venkateswara Rao, N., Balan, N., & Patra, A. K. (2014). Solar rotation effects on the Martian ionosphere. *Journal of Geophysical Research: Space Physics*, *119*, 6612–6622. <https://doi.org/10.1002/2014JA019894>

- Vogt, M. F., Withers, P., Fallows, K., Andersson, L., Girazian, Z., Mahaffy, P. R., ... Jakosky, B. M. (2017). MAVEN observations of dayside peak electron densities in the ionosphere of Mars. *Journal of Geophysical Research: Space Physics*, *122*, 891–906. <https://doi.org/10.1002/2016JA023473>
- Withers, P. (2009). A review of observed variability in the dayside ionosphere of Mars. *Advances in Space Research*, *44*, 277–307. <https://doi.org/10.1016/j.asr.2009.04.027>
- Withers, P., & Mendillo, M. (2005). Response of peak electron densities in the Martian ionosphere to day-to-day changes in solar flux due to solar rotation. *Planetary and Space Science*, *53*, 1401–1418. <https://doi.org/10.1016/j.pss.2005.07.010>
- Withers, P., Bougher, S. W., & Keating, G. M. (2003). The effects of topographically-controlled thermal tides in the Martian upper atmosphere as seen by the MGS accelerometer. *Icarus*, *164*, 14–32.
- Withers, P., Fillingim, M. O., Lillis, R. J., Häusler, B., Hinson, B. P., Tyler, G. L., ... Witasse, O. (2012). Observations of the nightside ionosphere of Mars by the Mars Express Radio Science Experiment (MaRS). *Journal of Geophysical Research: Space Physics*, *117*, A12307. <https://doi.org/10.1029/2012JA018185>
- Withers, P., Fallows, K., & Matta, M. (2014). Predictions of electron temperatures in the Mars ionosphere and their effects on electron densities. *Geophysical Research Letters*, *41*, 2681–2686. <https://doi.org/10.1002/2014GL059683>
- Withers, P., Morgan, D. D., & Gurnett, D. A. (2015). Variations in peak electron densities in the ionosphere of Mars over a full solar cycle. *Icarus*, *251*, 5–11. <https://doi.org/10.1016/j.icarus.2014.08.008>
- Zurek, R. W. (1988). Free and forced modes in the Martian atmosphere. *Journal of Geophysical Research*, *93*, 9452–9462.